ACS OMEGA

http://pubs.acs.org/journal/acsodf

Article

Tuning the Polarity of a Fibrous Poly(vinylidene fluoride-*co*-hexafluoropropylene)-Based Support for Efficient Water Electrolysis

Shunsaku Uchiyama,[+] Asuka Morinaga,[+] Hiromori Tsutsumi, and Yu Katayama*

Cite This: *ACS Omega* 2022, 7, 10077−10086

Read Online

ACCESS | Metrics & More | Article Recommendations | Supporting Information

ABSTRACT: Water electrolysis under alkaline conditions is of interest due to the applicability of non-precious metal-based materials for electrocatalysts. However, the successful design and synthesis of earth-abundant and efficient catalysts for the oxygen evolution reaction (OER) remain a significant challenge. This work presents cost-effective and straightforward ways to improve the OER activity under alkaline conditions by activating the catalyst−support and reactant−support interaction. Micro/nano-sized fibrous poly(vinylidene fluoride-*co*-hexafluoropropylene) (PVdF-HFP) was synthesized via simple and scalable electrospinning and subsequently coated with Cu by electroless deposition to obtain the electrocatalyst with a large specific surface area, enhanced mass transport, and high catalyst utilization. Scanning electron microscopy, infrared spectroscopy, and X-ray diffraction confirmed the successful synthesis of the series of Cu/PVdF-HFP fibrous catalysts with varied ferroelectric polarizability of the PVdF-HFP support in the order of stretch-anneal > anneal > stretch > without pre-treatment of the catalyst. The best OER activity was confirmed for the Cu/PVdF-HFP catalyst with stretch and annealed treatment among the catalysts tested, suggesting that both the reaction kinetics and energetics of stretch-annealed Cu/PVdF-HFP catalysts were optimal for the OER. The electron delocalization between Cu and PVdF-HFP substrates (electron transfer from Cu to the negatively charged (δ^-_{eff}) PVdF-HFP region at the CulPVdF-HFP interface) and the enhanced transport of reactive hydroxide species and/or the increase in the local pH by positively charged (δ^+_{eff}) PVdF-HFP region concertedly accelerate the OER activity. The overall activity for the prototype water electrolyzer increased 10-fold with stretch-anneal treatment compared to the one without pre-treatment, highlighting the effect of tuning the catalyst−support and reactant−support interaction on improving the efficiency of the water electrolysis.

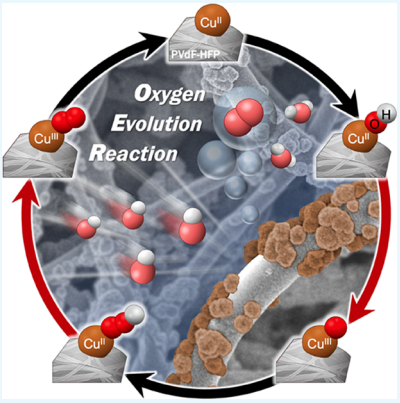

1. INTRODUCTION

Water electrolysis is one of the efficient and sustainable means to produce hydrogen, which is considered as a promising alternative to fossil-fuel-based energy sources, utilizing electricity generated from renewable sources, e.g., wind and solar.[1−4] The overall efficiency and cost of the water electrolyzer are critical in achieving mass production of hydrogen via water electrolysis. Typical water electrolyzers operate under acidic or alkaline conditions at temperatures up to 80 °C.[5,6] However, most non-precious metal-based catalysts gradually degrade in an acidic medium, and only precious metal-based catalysts can exhibit substantial stability.[7−9] Therefore, the study under an alkaline condition is essential to develop water electrolyzers with cost-effective, non-precious metal-based catalysts.

In water electrolyzers operated under alkaline conditions,[10,11] the hydrogen evolution reaction (HER, $2H_2O + 2e^- \rightleftarrows H_2 + 2OH^-$) and the oxygen evolution reaction (OER, $4OH^- \rightleftarrows O_2 + 2H_2O + 4e^-$) proceed at the cathode and anode, respectively. Although the HER has minimal energy losses,[12,13] the OER is a more complicated process with multiple-electron transfer, which requires a large overpotential and leads to a substantial energy loss,[14−16] even for the state-of-the-art OER catalyst (e.g., IrO_2[17,18] and RuO_2[17−19]). Furthermore, these electrocatalysts commonly contain precious metals such as Ir and Ru, and their high cost and scarcity impede the large-scale application. Design-efficient and durable OER electrocatalysts based on earth-abundant elements, e.g., 3d transition metals,[20,21] are thus crucial and have been investigated for more than decades.[7,22,23]

Among the 3d transition metals, Cu can be a potential candidate for the practical OER electrocatalysts due to its rich redox properties,[24,25] low cost,[26,25] and non-toxicity.[25] Recent studies successfully developed Cu-based OER catalysts with OER activity comparable to well-optimized Ni/Co-based catalysts[27−31] by tuning the energetics of the reaction intermediates via controlling sulfur content in Cu sulfide[32] or alloying with other 3d metals[33−35] or by adjusting the Cu

Received: November 1, 2021
Accepted: February 14, 2022
Published: March 14, 2022

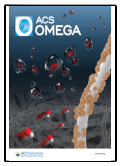

oxidation state under the OER potential with H_2O_2[36] or annealing[30,35] treatment of the Cu surface. Furthermore, for composite catalysts, such as nanoparticles deposited on a conductive support, successful control of the micro/macro-structure effectively increased the OER activity of Cu-based catalysts[31,37−39] by enhancing both mass transport and catalyst utilization.

In addition to active site engineering, designing the interactions between the catalyst atoms and support (catalyst−support interaction) plays a significant role in determining the stability and activity of catalysts.[40−44] The support provides a platform where the catalytic reaction occurs and defines the electronic structure of the catalyst atoms.[45,46] In this regard, to maximize the catalytic activity of Cu, optimizing the catalyst−support interaction is essential for the rational design of highly active Cu-based OER catalysts. Although the impact of the catalyst−support interaction on the OER activity has also been suggested for Cu-based catalysts,[47,48] insights into tuning the catalyst−support interaction to optimize the electronic structure are still insufficient and are further explored.

We present a simple pre-treatment of the catalyst, e.g., stretch and anneal treatment, which can effectively activate the catalyst−support and reactant−support interaction and improve the OER activity under alkaline conditions. The best OER activity was confirmed for highly polarized Cu/PVdF-HFP catalysts with stretch and anneal treatment among the catalysts tested, suggesting that the reaction kinetics and energetics of the OER was optimized by the simple stretch and annealing treatment. We propose that the positively charged (δ^+_{eff}) PVdF-HFP region facilitates the transport of reactive hydroxide species, while the electron transfer from Cu to the negatively charged (δ^-_{eff}) PVdF-HFP region at the Cu|PVdF-HFP interface accelerates the rate-determining step of the OER. A more than 10-fold increase in the overall performance was confirmed for a prototype water electrolyzer consisting of the bi-functional membrane electrode assembly with stretch-anneal treatment compared to the one without pre-treatment, further validating the effect of tuning the catalyst−support and reactant−support interaction on increasing the OER performance. Our findings provide a new design strategy for a highly active OER catalyst, whereby the OER activity can be increased by designing the active metal site and tuning the catalyst−support and reactant−support interaction.

2. EXPERIMENTAL SECTION

2.1. Electrocatalyst Preparation. The Cu-deposited fibrous electrode was prepared by the electrospinning method reported elsewhere.[47] The electrospinning solution consisted of a THF and DMF mixture (7:3 by vol) containing 10 mg of $PdCl_2$ (Wako Pure Chemical) with 12 wt % of poly(vinylidene fluoride-*co*-hexafluoropropylene) (PVDF-HFP, average molecular weight = 400,000). Electrospinning was performed using electrospinning equipment (NANON-03, MECC Co. Ltd.) at an applied voltage of 28 kV with a feeding rate of 1 mL h^{-1} while rotating a drum-shaped collector along the rotating axis at 3000 rpm. The distance between the injector and the collector was set to 10 cm. The resultant fibers were dried at room temperature for 24 h under reduced pressure (*ca.* 400 Pa) to remove the organic residue. In order to vary the ferroelectric polarizability of PVDF-HFP/$PdCl_2$ fibers, the obtained fibers were mechanically stretched and/or annealed. PVDF-HFP/ $PdCl_2$ fibers were mechanically stretched up to 150% along with the fiber at room temperature (denoted as PVDF-$HFP_{stretch}$). Both pristine and stretched PVDF-HFP/$PdCl_2$ fibers were annealed at 140 °C for *ca.* 2 h under an atomosphere[49,50] (denoted as PVDF-HFP/$PdCl_{2\ anneal}$ and PVDF-HFP/$PdCl_{2stretch\text{-}anneal}$, respectively). Subsequently, Cu electroless deposition was performed by immersing the resultant electrodes into the Cu plating solution, consisting of $CuSO_4{\cdot}5H_2O$ (0.80 g, Wako Pure Chemical), ethylenediaminetetraacetic acid (1.46 g, Nacalai Tesque), NaOH (2.0 g, Wako Pure Chemical), HCHO (0.5 mL, Wako Pure Chemical), and ultrapure water, at 40 °C for *ca.* 15 min. The Cu-deposited PVdF-HFP, Cu-deposited PVdF-$HFP_{stretch}$, Cu-deposited PVdF-HFP_{anneal}, and Cu-deposited PVdF-$HFP_{stretch\text{-}anneal}$ fibers are represented as Cu/PVdF-HFP, Cu/PVdF-$HFP_{stretch}$, Cu/ PVdF-HFP_{anneal}, and Cu/PVdF-$HFP_{stretch\text{-}anneal}$, respectively.

2.2. Fabrication of Bi-functional Membrane Electrode Assembly. A multilayered fiber (PVdF-HFP/$PdCl_2$|PVdF-HFP|PVdF-HFP/$PdCl_2$) was synthesized using the setup mentioned above with multiple electrospinning of different electrospinning solutions. First, PVdF-HFP/$PdCl_2$ was synthesized using the electrospinning solution with the same composition described in Section 2.1. The PVdF-HFP was then synthesized over the PVdF-HFP/$PdCl_2$ fiber using the electrospinning solution without the $PdCl_2$ additive. Finally, the multilayered fiber of PVdF-HFP/$PdCl_2$|PVdF-HFP|PVdF-HFP/$PdCl_2$ was obtained by the electrospinning using the electrospinning solution with the $PdCl_2$ additive over the PVdF-HFP/$PdCl_2$|PVdF-HFP fiber. The obtained multilayered fiber was dried at room temperature for 24 h under a reduced pressure (*ca.* 400 Pa) followed by Cu electroless deposition in the same manner described in Section 2.1.

2.3. Characterization. The microstructure of all Cu/PVdF-HFP catalysts was analyzed by a scanning electron microscope (SEM, JSM-7600F, JEOL Ltd. with an accelerating voltage of 20 kV) equipped with an energy-dispersive X-ray spectrometer (EDS, JMS-7600F, JEOL Ltd.). The X-ray diffraction (XRD) patterns of Cu/PVdF-HFP catalysts were obtained by an X-ray diffractometer (Rigaku Ultima IV) with Cu Kα radiation. X-ray photoelectron spectroscopy (XPS) was performed on the K-Alpha spectrometer (Thermo Fischer Scientific). XPS spectra were calibrated by adventitious carbon at 284.8 eV (C 1s spectra). After subtraction of a Shirley-type background, the photoemission lines were fitted using combined Gaussian−Lorentzian functions. Electrochemical cleaning of the electrode was performed in a standard three-electrode cell and by cycling the potential between −0.9 and 1.8 V vs reversible hydrogen electrode (potential cycling was terminated at 1.8 V after 10 cycles). The infrared spectra of the materials were obtained on a Nicolet iS50 (Thermo Fischer Scientific) equipped with a deuterated triglycine sulfate (DTGS) detector. A single reflection attenuated total reflection (ATR) accessory (Smart iTX, Thermo Fischer Scientific) with a ZnSe prism was used to obtain the spectra. The ATR measurements were performed at an incident angle of 45° with a 4 cm^{-1} resolution. The spectra were collected in the wavenumber range 4000−500 cm^{-1} with a cumulative number of 64. All spectra are shown in the absorbance units defined as $\log(I_0/I)$, where I_0 and I represent the background spectra and sample spectra, respectively. The background spectrum I_0 was measured without any sample.

2.4. Electrochemical Measurements. Electrochemical measurements were carried out on an HZ-5000 potentiostat

https://doi.org/10.1021/acsomega.1c06128
ACS Omega 2022, 7, 10077−10086

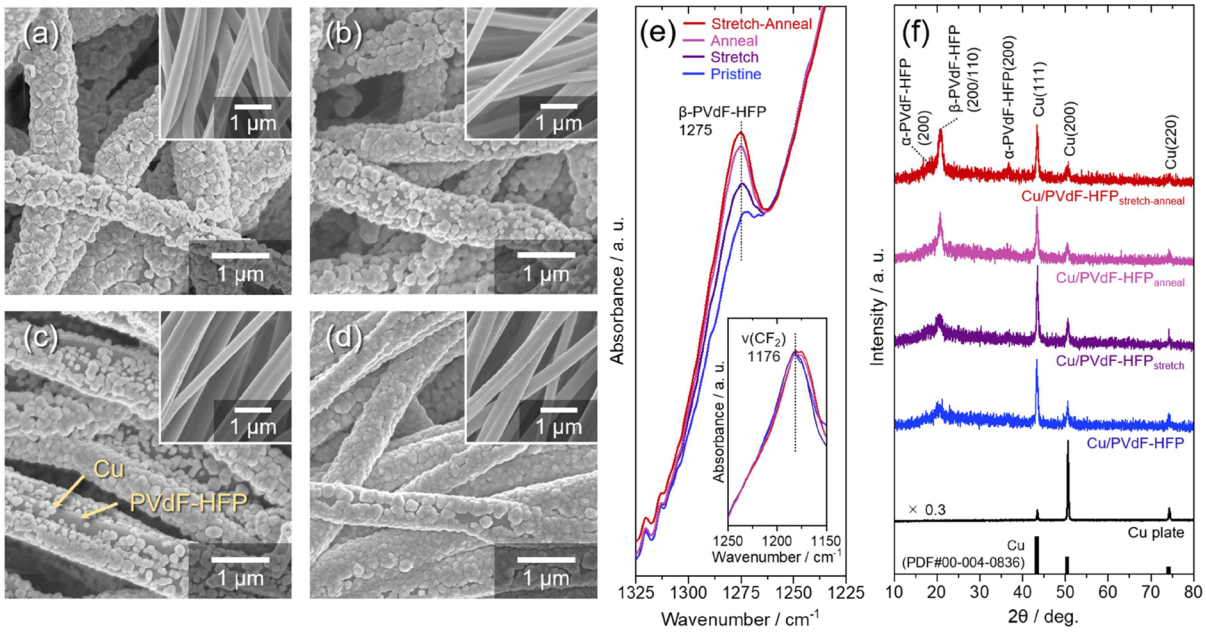

Figure 1. Characterization of the Cu/PVdF-HFP catalysts with various pre-treatments. SEM images of (a) pristine, (b) stretched, (c) annealed, and (d) stretch-annealed PVdF-HFP/$PdCl_2$ fibers after Cu electroless deposition. The inset shows the corresponding SEM images before Cu electroless deposition. (e) Infrared spectra for pristine, stretched, annealed, and stretch-annealed PVdF-HFP/$PdCl_2$ fibers before Cu electroless deposition. The spectra were normalized by the intensity of the CF_2 stretching peak at 1176 cm^{-1}[53,54] shown in the inset. (f) XRD patterns of Cu/PVdF-HFP, Cu/PVdF-$HFP_{stretch}$, Cu/PVdF-HFP_{anneal}, and Cu/PVdF-$HFP_{stretch\text{-}anneal}$ fibers. XRD patterns of the Cu plate and standard Cu (PDF #00-004-0836) are shown for comparison.

(Hokuto Denko) at room temperature. The cyclic voltammogram (CV) and linear sweep voltammogram (LSV) were obtained in a standard three-electrode cell with a Pt wire counter electrode and Ag/AgCl reference electrode. The overall performance of the water electrolysis was evaluated using a two-electrode configuration, and the chronoamperometric curve was recorded at an applied voltage of 2.5 V. The electrolyte solution was prepared by mixing KOH (Wako Pure Chemical, >85 wt %) and ultrapure water (Nihon Millipore K.K). Before every experiment, argon was bubbled through the electrolyte for at least 15 min to completely deoxygenate the solution. The electrode was cleaned by cycling the potential between −0.05 and 1.50 V versus the reversible hydrogen electrode (RHE) before the measurement. All potentials reported here are referenced to the RHE scale (expressed as V_{RHE}). The ECSA for the series of the Cu/PVdF-HFP fiber was determined following a similar procedure previously reported.[51,52] In short, ECSA (A) was calculated from the peak oxidation current (I_p) related to $Cu(OH)_2$ formation using the following equation: $A = 3525.8 \times I_p$. The peak oxidation current was obtained by linear sweep voltammetry at a scan rate of 10 mV/s in an Ar-purged KOH electrolyte (see Figure S1 for the LSV and obtained ECSA). The current density was obtained by normalizing the current to the ECSA (expressed as $\mu A\ cm^{-2}_{ECSA}$) unless otherwise noted.

3. RESULTS AND DISCUSSION

The successful synthesis of a series of Cu/PVdF-HFP fibrous catalysts was confirmed by scanning electron microscopy (SEM), infrared (IR) spectroscopy, and XRD, suggesting uniform Cu nanoparticle deposition for all the catalysts as well as diverse ferroelectric polarizability of PVdF-HFP substrates by annealing and/or stretching treatment (Figure 1).

The SEM images confirm that all the pristine PVdF-HFP/$PdCl_2$ fibers, prepared by the electrospinning method with and without annealing and/or stretching treatment, possess a similar morphology with a fiber diameter of *ca.* 0.47 μm (Figure 1a–d, inset). After electroless deposition of Cu, the smooth surface of the PVdF-HFP substrate was covered by a particle-like deposit, in line with the increase in the average diameter of *ca.* 0.66 μm (Figure 1a–d). The energy-dispersive X-ray spectroscopy (EDS) identified the deposit as a Cu particle, which confirms the successful synthesis of the series of Cu/PVdF-HFP fibrous catalysts (Figure S2). Note that the Cu deposit (a light gray area in the SEM) did not fully cover the fiber surface, and the PVdF-HFP substrate was partially exposed (a dark gray area in the SEM). However, the obtained Cu/PVdF-HFP fibrous catalysts showed good electrical conductivity, suggesting that the Cu particle connected well enough to create the electron-conducting path. The high void volume observed for all the Cu/PVdF-HFP fibers contributes to the efficient mass transfer of reactant and product molecules.[47]

Infrared spectra of pristine PVdF-HFP/$PdCl_2$ fibers showed distinctive features corresponding to β-phase PVdF-HFP at *ca.* 1275 cm^{-1},[53,54] suggesting the increased β-phase PVdF-HFP population in the following order: stretch-anneal > anneal > stretch > pristine (Figure 1e). The ferroelectric polarizability is in line with the amount of β-phase PVdF-HFP due to the following reasons: The β-phase PVdF-HFP has an orthorhombic structure and an all-trans molecule conformation, leading to alignment of the dipoles ($-CH_2CF_2-$) perpendicular to the chain axis (Figure S3).[55,56] Therefore, the β-phase PVdF-HFP possesses a large spontaneous polarization, which evokes the characteristic ferroelectricity of PVDF and its copolymers. We thus conclude that the ferroelectric polarizability of PVdF-HFP can be tuned by the simple annealing

https://doi.org/10.1021/acsomega.1c06128
ACS Omega 2022, 7, 10077−10086

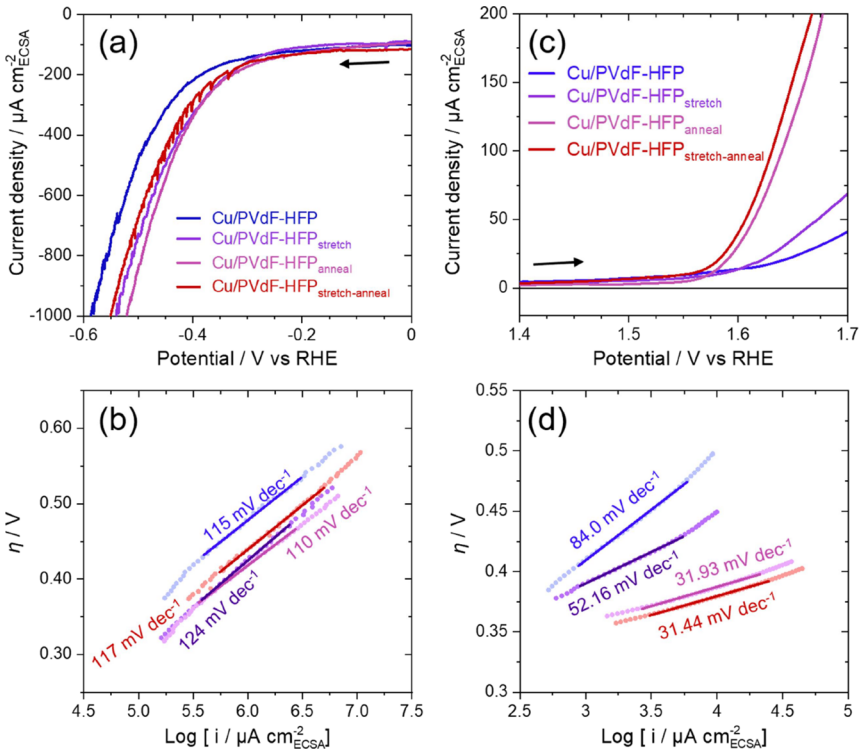

Figure 2. Comparison of the HER and OER activity of the catalysts. (a, c) Linear sweep voltammograms for Cu/PVdF-HFP, Cu/PVdF-HFP$_{stretch}$, Cu/PVdF-HFP$_{anneal}$, and Cu/PVdF-HFP$_{stretch-anneal}$ catalysts in 1.0 M KOH at a scan rate of 0.1 mV s^{-1}. (b, d) Corresponding Tafel plots for Cu/PVdF-HFP, Cu/PVdF-HFP$_{stretch}$, Cu/PVdF-HFP$_{anneal}$, and Cu/PVdF-HFP$_{stretch-anneal}$ catalysts in 1.0 M KOH. The Tafel slope of each electrode is indicated.

and/or stretching treatment, resulting in the ferroelectric polarizability in the following order: Cu/PVdF- HFP$_{stretch-anneal}$ > Cu/PVdF-HFP$_{anneal}$ > Cu/PVdF-HFP$_{stretch}$ > Cu/PVdF-HFP.

XRD patterns of the series of Cu/PVdF-HFP catalysts further supports the varied ferroelectric polarizability and deposition of Cu particles (Figure 1f). The characteristic XRD peak corresponds to the β-phase PVdF-HFP appeared at *ca.* 21° (200/110),[52,57] which gradually increased its intensity and shifted to a higher degree after annealing and/or stretching treatment, indicating the formation of a metastable β-phase by those simple treatments (XRD patterns of the pre-treated PVdF-HFP support without Cu deposition are shown in Figure S4). The XRD patterns also showed diffraction peaks corresponding to Cu, confirming the successful deposition of Cu on all Cu/PVdF-HFP catalysts. Note that Cu/PVdF-HFP catalysts are in the form of thin films, and the flexibility of the pristine PVdF-HFP/$PdCl_2$ fiber is still maintained after Cu deposition.

The electrocatalytic activity toward the oxygen evolution reaction (OER) was clearly improved by the annealing and/or stretching treatment, while the hydrogen evolution reaction (HER) activity only showed slight improvement by the pre-treatment of the catalysts (Figure 2).

The linear sweep voltammogram showed the similar HER current of *ca.* −500 μA cm^{-2} at −0.45 V_{RHE} for the catalysts with pre-treatment (Cu/PVdF-HFP$_{stretch}$, Cu/PVdF-HFP$_{anneal}$, and Cu/PVdF-HFP$_{stretch-anneal}$), which was slightly larger than that of pristine Cu/PVdF-HFP (*ca.* −300 μA cm^{-2} at −0.45 V_{RHE}) (Figure 2a). The onset potential of the HER also showed a similar trend, where the catalysts with pre-treatment required slightly smaller (<0.1 V) overpotential to initiate HER compared to the pristine catalyst. The Tafel slope value was *ca.* 120 mV dec^{-1} regardless of the pre-treatment (Figure 2b), indicating that the initial Volmer step (water dissociation: $H_2O + e^- \rightarrow H_{ad} + OH^-$)[58,59] could be the rate-determining step of the HER for the catalysts used in this study. From the above observations, we concluded that the change in the ferroelectric polarizability of the PVdF-HFP support slightly improved the HER activity. We here propose that the increased ferroelectric polarizability of the PVdF-HFP support lowers the water dissociation energy barrier (responsible for the rate-determining step for the HER in alkaline electrolytes)[60] by stabilizing the metal-OH-water (M-OH_{ad}-H_2O_{ad}) complex due to the increased hydrophilicity[61] (discussed further in the later paragraph).

The specific OER current of Cu/PVdF-HFP$_{stretch-anneal}$, Cu/PVdF-HFP$_{anneal}$, and Cu/PVdF-HFP$_{stretch}$ catalysts at 1.65 V_{RHE} showed *ca.* 6.9-, 5.4-, and a 1.6-fold increase compared to that of the pristine Cu/PVdF-HFP catalyst, respectively (Figure 2c). Furthermore, the OER current at a relatively large overpotential region (>1.7 V_{RHE}) observed for Cu/PVdF-HFP$_{anneal}$ and Cu/PVdF-HFP$_{stretch-anneal}$ showed a steeper slope compared to that of Cu/PVdF-HFP$_{stretch}$ and pristine Cu/PVdF-HFP. The result indicates the enhanced diffusion of the reactant and/or the product for catalysts with stretch-anneal and anneal treatments. Although the high void volume of the fibrous structure improves the mass transfer of reactant and product molecules and partial exposure of hydrophobic PVdF-HFP substrate assists the removal of the reaction product (oxygen gas) from the surface,[47] both of which cannot be the reason for the steep slope of the LSV at the large overpotential region for catalysts with stretch-anneal and anneal treatments. We here propose that the ferroelectric polarizability of PVdF-

https://doi.org/10.1021/acsomega.1c06128
ACS Omega 2022, 7, 10077−10086

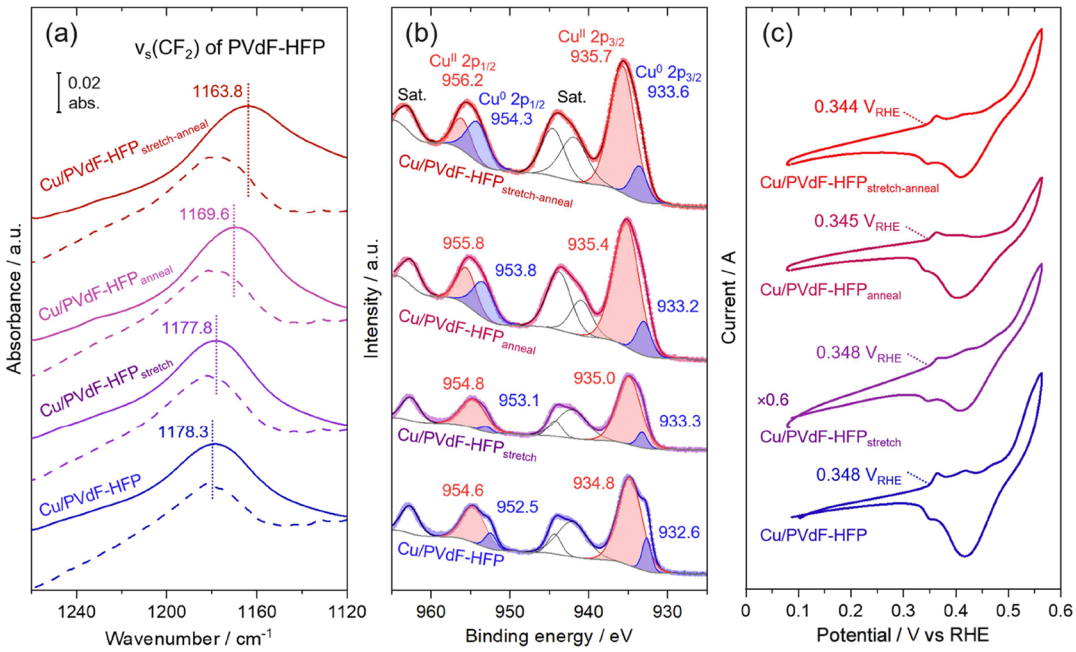

Figure 3. Synergetic effect between Cu and PVdF-HFP. (a) ATR-IR spectra of C−F stretching region for Cu/PVdF-HFP, Cu/PVdF-HFP$_{stretch}$, Cu/PVdF-HFP$_{anneal}$, and Cu/PVdF-HFP$_{stretch\text{-}anneal}$ catalysts. The broken line shows corresponding PVdF-HFP/$PdCl_2$ fibers before Cu electroless deposition. (b) XPS spectra of the Cu 2p photoemission lines for Cu/PVdF-HFP, Cu/PVdF-HFP$_{stretch}$, Cu/PVdF-HFP$_{anneal}$, and Cu/PVdF-HFP$_{stretch\text{-}anneal}$ catalysts. All spectra were calibrated to the adventitious carbon at 284.8 eV and background-corrected using a Shirley background. Cu 2p spectra were assigned with the following contributions: Cu^0 (~932.6 eV)[64,65] and Cu^{II} (~934.8 eV).[64,66] C 1s XPS spectra are shown in Figure S9. (c) Cyclic voltammograms of Cu/PVdF-HFP, Cu/PVdF-HFP$_{stretch}$, Cu/PVdF-HFP$_{anneal}$, and Cu/PVdF-HFP$_{stretch\text{-}anneal}$ catalysts in 1.0 M KOH at a scan rate of 50 mV s^{-1}.

HFP effectively anchors negatively charged OH^- at the vicinity of the electrode, accelerating the OH supply to the Cu active sites. The hypothesis is supported by the fact that OER activation by stretch-anneal treatment was not observed for the comparable fibrous Cu/polystyrene (Cu/PS) catalyst without ferroelectricity (Figure S5). Although the polarized PVdF-HFP surface possesses both positive and negative charges depending on the CH_2/CF_2 orientation,[62] negatively charged PVdF-HFP (surface with CF_2 dipoles (δ^-_{eff})) might preferentially be covered by Cu since it attracts Cu^{2+} during the electroless deposition process. The electrostatic interaction between the positively charged PVdF-HFP surface by CH_2 dipoles (δ^+_{eff}) and negatively charged OH^- anchors the OH^- close to the electrode surface. Linear sweep voltammograms in various KOH concentrations further support our hypothesis (Figure S6). The OER current became more extensive along with the increase in the KOH concentration (from 1 to 2 M KOH) for pristine electrodes, suggesting the enhancement of OER by the increased amount of OH^- active species. The OER current for the catalyst with stretch-anneal treatment obtained in 1 M KOH was notably more significant than that for the pristine electrode in 2 M KOH, suggesting the high local concentration (>2 M) of OH^- achieved by the enhanced ferroelectric polarizability of the PVdF-HFP support.

All the pre-treated Cu/PVdF-HFP catalysts exhibit superior specific OER activity compared to that of the pristine catalyst, with an overpotential (η) of 370 mV (stretch-anneal) < 380 mV (anneal) < 440 mV (stretch) < 490 mV (pristine) to reach 50 μA cm^{-2}_{ECSA} (Figure 2d). In addition, the Nyquist plot of the Cu/PVdF-HFP$_{stretch\text{-}anneal}$ catalyst shows a smaller charge transfer resistance than that of pristine Cu/PVdF-HFP, demonstrating the enhanced charge transfer kinetics (Figure S7).[63] Tafel analysis further confirms the activation of OER for the Cu/PVdF-HFP$_{stretch\text{-}anneal}$ catalyst, showing the smallest Tafel slope value of 31 mV dec^{-1} followed by Cu/PVdF-HFP$_{anneal}$ (32 mV dec^{-1}), Cu/PVdF-HFP$_{stretch}$ (52 mV dec^{-1}), and pristine (84 mV dec^{-1}) catalysts. The Tafel slope value slightly decreased from *ca.* 84 mV dec^{-1} (1 M KOH) to 58 mV dec^{-1} (2 M KOH) with increasing the KOH concentration for the pristine catalyst (Figure S8), suggesting that the enhanced OH supply to the Cu active sites and/or the increase in pH at the vicinity of the electrode surface can be part of the reasons for the improved specific OER activity. However, a significant decrease in the Tafel slope value, as well as the overpotential observed for the catalyst with stretch-anneal treatment, cannot be explained only by the increase in the OH^- concentration. We propose that the synergetic effect between Cu and PVdF-HFP (electron transfer from Cu to PVdF-HFPField 47) at the Cu|PVdF-HFP interface varies with the pre-treatment and optimizes reaction energetics for OER.

Attenuated total reflection infrared (ATR-IR) spectroscopy and *ex situ* XPS revealed that the electron delocalization between Cu and PVdF-HFP substrates was promoted for the catalyst with increased ferroelectric polarizability of the PVdF-HFP support. The electron transfer from Cu to PVdF-HFP alters the electronic states of Cu active sites, boosting OH binding on the Cu, especially for the Cu/PVdF-HFP$_{stretch\text{-}anneal}$ (Figure 3).

A clear redshift of the $\nu_s(CF_2)$ band was observed for Cu-deposited PVDF-HFP catalysts with respect to the corresponding PVDF-HFP/$PdCl_2$ fibers (before Cu deposition) confirms the existence of the electrostatic interaction between Cu and PVDF-HFP (Figure 3a). The amount of wavenumber shift depends on the pre-treatment; Cu/PVdF-HFP$_{stretch\text{-}anneal}$ (Δ14.4 cm^{-1}) > Cu/PVdF-HFP$_{anneal}$ (Δ8.6 cm^{-1}) > Cu/PVdF-HFP$_{stretch}$ (Δ2.2 cm^{-1}) = pristine Cu/PVdF-HFP (Δ1.7

https://doi.org/10.1021/acsomega.1c06128
ACS Omega 2022, 7, 10077−10086

cm^{-1}), indicating the degree of electrostatic interaction between CF_2 dipoles (δ^-_{eff}) with Cu varies with ferroelectric polarizability of the PVdF-HFP support. We propose that well-aligned CF_2 dipoles (δ^-_{eff}) within β-phase PVdF-HFP interact with Cu and its large δ^-_{eff} strongly withdraws electron from Cu. Furthermore, the negatively charged PVDF-HFP region (surface with CF_2 dipoles (δ^-_{eff})) can effectively interact with Cu since the negatively charged region is mostly covered by Cu owing to the preferential attraction of the positively charged Cu^{2+} during the electroless deposition process.

The electron transfer from Cu to the PVdF-HFP substrate can also be suggested from Cu 2p spectra of the electrochemically cleaned Cu/PVdF-HFP catalysts (Figure 3b). The Cu 2p XPS spectra showed two asymmetric bands, which could be deconvoluted into two pairs of doublets assigned to Cu^0 (932.6–933.6 and 952.5–954.3 eV)[64,65] and Cu^{II} (934.8–935.7 and 954.6–956.2 eV).[64,66] The contribution from Cu^{II} (934.8–935.7 and 954.6–956.2 eV) was dominant for all the catalysts tested, indicating that the Cu mainly exists as Cu^{II} in the Cu/PVdF-HFP fiber surfaces after electrochemical cleaning. CuO formation was also confirmed by comparing the XRD patterns before and after the OER, further emphasizing the importance of Cu^{II} on the OER (Figure S10). The Cu^{II} peaks shifted to a higher binding energy in line with the increase in the ferroelectric polarizability of the PVdF-HFP support: Cu/PVdF-$HFP_{stretch\text{-}anneal}$ (935.7, 956.2 eV) > Cu/ PVdF-HFP_{anneal} (935.4, 955.8 eV) > Cu/PVdF-$HFP_{stretch}$ (935.0, 954.8 eV) = pristine Cu/PVdF-HFP (934.8, 954.6 eV). The positive shift in binding energies of Cu^{II} peaks implies the electron deficiency of the Cu sites, which supports the existence of the electron transfer from Cu to PVdF-HFP.[40] Furthermore, the trend in the binding energy of the Cu^{II} peak coincides with the wavenumber shift of the $\nu_s(CF_2)$ band, strongly indicating that the electron transfer from Cu to PVdF-HFP can be accelerated by increasing the ferroelectric polarizability of PVdF-HFP.

The electron transfer from Cu to PVdF-HFP affects the binding energetics of the O/OH adsorbates, which can be confirmed by comparing the onset potential of the O/OH adsorption (Figure 3c). Cyclic voltammograms showed butterfly features at *ca.* 0.35 V_{RHE}, corresponding to the O/OH adsorption/desorption on the Cu(100) facet.[67,68] The onset potential of the O/OH adsorption shifted to a lower potential by increasing the ferroelectric polarizability of the PVdF-HFP support: pristine Cu/PVdF-HFP (0.348 V_{RHE}) = Cu/PVdF-$HFP_{stretch}$ (0.348 V_{RHE}) > Cu/PVdF-HFP_{anneal} (0.345 V_{RHE}) > Cu/PVdF-$HFP_{stretch\text{-}anneal}$ (0.344 V_{RHE}). The trend suggests the strong O/OH binding for the Cu on the highly polarized PVdF-HFP support, which is in accordance with the degree of the electron transfer from Cu to the PVdF-HFP substrate (Figure 3b).

The Cu/PVdF-HFP catalyst with stretch-anneal treatment showed the best OER activity among the catalysts tested, suggesting that both the reaction kinetics and energetics of the Cu/PVdF-$HFP_{stretch\text{-}anneal}$ catalysts were optimal for OER. The positively charged (δ^+_{eff}) PVDF-HFP region facilitates the transport of reactive hydroxide species, while the electron transfer from Cu to the negatively charged (δ^-_{eff}) PVdF-HFP region at the Cu|PVdF-HFP interface accelerates the rate-determining step of the OER (Figure 4).

The highly polarized PVdF-HFP substrate with stretch-anneal treatment possesses both positive and negative charges depending on the CH_2/CF_2 orientation. Negatively charged

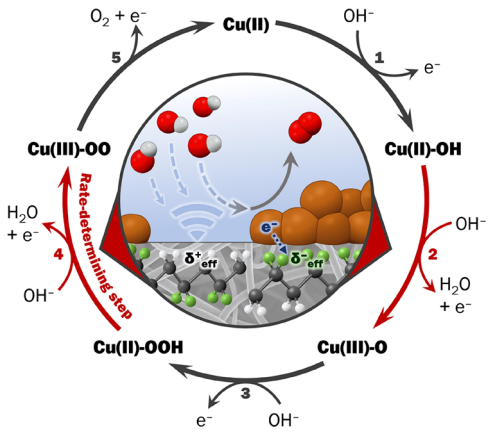

Figure 4. Proposed reaction mechanism for the electrochemical oxygen evolution reaction on Cu under basic conditions. The positively charged (δ^+_{eff}) PVDF-HFP region by CH_2 dipoles electrostatically attracts hydroxyl species at the vicinity of the surface. The negatively charged (δ^-_{eff}) region of the PVdF-HFP support effectively withdraws the electron from Cu sites, leading to form electron-deficient Cu sites. The electron-deficient Cu sites promote the rate-determining step of the OER, resulting in the highest OER activity for the highly polarized catalyst with stretch-anneal treatment.

PVDF-HFP (surface with CF_2 dipoles (δ^-_{eff})) mostly covered by Cu owing to the electrostatic attraction between δ^-_{eff} and positively charged Cu^{2+} during the electroless deposition process. The large electronegativity of the F atom effectively withdraws the electron from Cu to PVdF-HFP, creating a slightly electron-deficient Cu site. Stronger O/OH binding on the slightly electron-deficient Cu site than the normal Cu site promotes the initial hydroxide adsorption and the subsequent deprotonation of OH_{ad} to form O_{ad}, which agrees with the CVs in Figure 3c. Furthermore, the electrophilicity of the oxygen adsorbates (O_{ad}) on the slightly electron-deficient Cu site can be increased, promoting the formation of the OOH_{ad} via nucleophilic attack from OH^- within the electrolyte.[36] The fourth electron transfer reaction of the OER (deprotonation of OOH_{ad} to form OO_{ad}) can also be facilitated through the electron-withdrawing inductive effect,[43,71] which accelerates the overall OER activity (Figure 4).[69,70] Tafel analysis of the stretch-annealed Cu-deposited PVDF-HFP catalyst further supports our hypothesis (Figure 2d). The Tafel slope (b) can be expressed as eq 1, where η is the overpotential, i is the current density, R is the universal gas constant, T denotes the absolute temperature, F is the Faraday constant, and α is the transfer coefficient

$$b = \frac{\partial \eta}{\partial \log(i)} = \frac{2.303RT}{\alpha F} \quad (1)$$

The transfer coefficient (α) for a multiple-electron reaction[72] is shown in eq 2, where n_b is the number of electrons that transfer back to the electrode before the rate-determining step, ν is the number of rate-determining steps that have taken place in the overall reaction, n_r is the number of electrons that participate in the rate-determining step, and β is the symmetry factor (β = 0.5 in this study, assuming that overpotential is much smaller than the reorganization energy).

$$\alpha = \frac{n_b}{\nu} + n_r\beta \quad (2)$$

https://doi.org/10.1021/acsomega.1c06128
ACS Omega 2022, 7, 10077−10086

A Tafel slope value of 31 mV dec^{-1} for stretch-annealed catalysts thus suggests $n_b = 3$ and $\nu = 2$, which translated into the fact that the second (deprotonation of OH_{ad} to form O_{ad}) and fourth (deprotonation of OOH_{ad} to form OO_{ad}) electron transfer reactions can be the sluggish (energetically unfavorable) process ($\nu = 2$), and the fourth reaction acts as a major rate-determining step ($n_b = 3$). The proposed rate-determining step agrees with the proposed OER energetics on Cu,[73,74] further validating our Tafel analysis. The Tafel slope value varies between 31 and 84 depending on the pre-treatment of the PVdF-HFP substrate, probably due to the change in the OER energetics and/or the existence of the mixed rate-determining step.

On the other hand, positively charged PVdF-HFP (surface with CH_2 dipoles (δ^+_{eff})) was preferably exposed to the electrolyte due to the electrostatic repulsion, which prevents the reduction of Cu^{2+} during the electroless deposition process. The electrostatic attraction between δ^+_{eff} of the exposed PVdF-HFP surface and negatively charged OH^- in the electrolyte may promote (1) the diffusion of the OH^- toward the electrode and/or (2) increase the local pH at the vicinity of the surface. The former facilitates the diffusion kinetics of the reactant (OH^-) together with the unique fibrous structure of the substrate, while the latter improves the reaction energetics of the OER.[40,75,76]

The unique interaction between Cu and PVdF-HFP with stretch-anneal treatment may strongly influence its activity for overall water electrolysis. The overall performance of the water electrolyzer consisting of the bi-functional membrane electrode assembly (MEA), Cu/PVdF-HFP|PVdF-HFP|Cu/PVdF-HFP, with stretch-anneal treatment was significantly improved in comparison with a pristine bi-functional MEA, together with the high (electro)chemical stability for more than 24 h (Figure 5).

The bi-functional membrane electrode assembly (MEA) was synthesized by a simple two-step process, electrospinning, and subsequent Cu electrodeposition, without slurry synthesis and/or screen printing of the catalyst, which was involved in the conventional MEA manufacturing process. The resultant bi-functional MEA is a single flexible sheet with a thickness of *ca.* 0.5 mm (Figure 5a,b). The cross-sectional image confirms that the top and bottom Cu-deposited layers (Cu/PVdF-HFP) are tightly attached to the PVdF-HFP layer (middle layer), and it is electrically separated from each other (Figure 5c,d). To evaluate the effect of pre-treatment on the stability and activity of the Bi-functional MEA, a water electrolyzer consisting of bi-functional MEA with and without stretch-anneal treatment was operated under a potentiostatic mode at an applied voltage of 2.5 V in 1 M KOH. As plotted in Figure 5e, both bi-functional MEAs exhibit a slight activity decay in the first 16 h of operation, subsequently representing a stable horizontal line up to 28 h. The cycling stability test suggests that the initial activity decay can be due to the partial aggregation of the Cu particles, which was confirmed by XRD, XPS, and SEM analyses (Figure S11). A more than 10-fold increase in the current was observed for the bi-functional MEAs with stretch-anneal treatment (9.63 mA cm^{-2} at 28 h) compared to that without pre-treatment (0.63 mA cm^{-2} at 28 h), demonstrating the outstanding improvement in the overall performance for the water electrolysis by the simple stretch and anneal treatment.

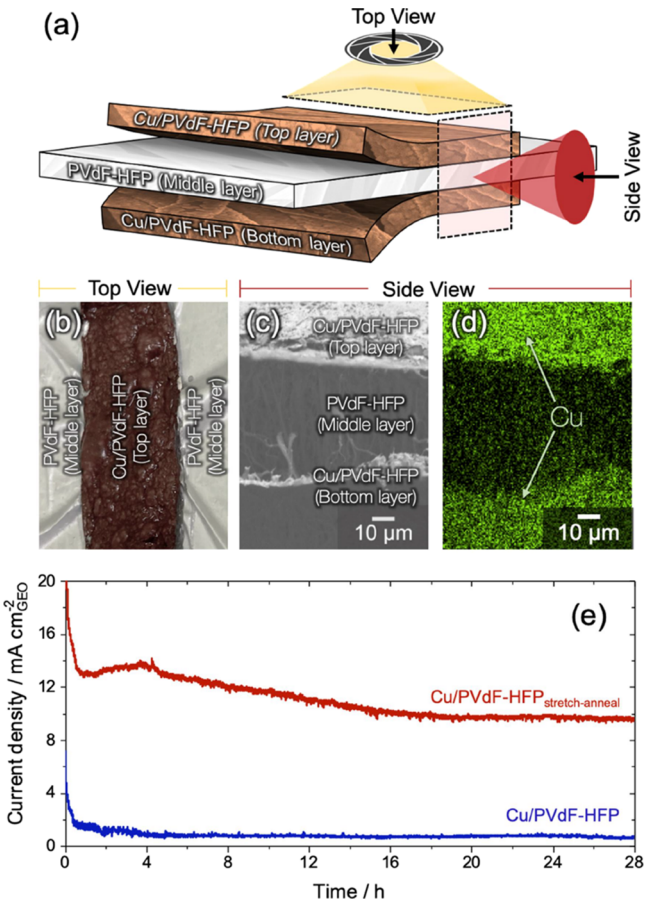

Figure 5. Bi-functional membrane electrode assembly for water electrolyzers. (a) Schematics of the prepared bi-functional membrane electrode assembly. Representative (b) photograph of the top-view and cross-sectional (c) SEM and (d) EDX images of the bi-functional membrane electrode assembly. (e) Long-term durability tests for the water electrolyzer consisting of the bi-functional membrane electrode assembly (Cu/PVdF-HFP|PVdF-HFP|Cu/PVdF-HFP) with and without stretch-anneal treatment at an operation voltage of 2.5 V.

4. CONCLUSIONS

In this work, the oxygen evolution reaction activity on Cu in alkaline environments was significantly increased by activating the catalyst−support and reactant−support interaction via simple pre-treatment of the Cu-deposited fibrous PVdF-HFP catalysts. The ferroelectric polarizability of the PVdF-HFP support is successfully tuned by simple pre-treatment, leading to the increased population of the highly polarized β-PVdF-HFP in the following order: stretch, anneal, and stretch-anneal treatment. The electron transfer from Cu to PVdF-HFP was accelerated in line with the polarizability of the PVdF-HFP support, which was supported by the redshift of the $\nu_s(CF_2)$ band and the positive shift in binding energies of Cu^{II} peaks of the ATR-IR and XPS spectra, respectively. The Cu/PVdF-HFP catalyst with stretch and anneal treatment showed the best OER activity among the catalyst tested, suggesting that both the reaction kinetics and energetics of Cu/PVdF-$HFP_{stretch-anneal}$ catalysts were optimal for the OER. The increased OER activity for the Cu/PVdF-$HFP_{stretch-anneal}$ catalyst can be attributed to the (1) facile transport of reactive hydroxide species and increased local pH by the electrostatic interaction between the positively charged (δ^+_{eff}) PVdF-HFP region and hydroxide ions and (2) the acceleration of the rate-

https://doi.org/10.1021/acsomega.1c06128
ACS Omega 2022, 7, 10077−10086

determining step of the OER (deprotonation of OOH_{ad} to form OO_{ad}) by the electron transfer from Cu to the negatively charged (δ^-_{eff}) PVdF-HFP region at the CulPVdF-HFP interface. The performance of the prototype water electrolyzer consisting of bi-functional membrane electrode assembly was significantly increased by stretch-anneal treatment, further validating the impact of tuning the catalyst−support and reactant−support interaction on the performance of the water electrolysis. The abovementioned interactions can be adjusted by simple pre-treatment with stretch and anneal, leading to aligning the molecular structure and increasing the polarity of the polymer substrate. Furthermore, the proposed pre-treatment, as well as the synthesis procedures for the flexible and durable membrane electrode assembly, is simple and scalable, which not only expands the applicability of the water electrolyzer but also opens up a new avenue to fabricate the membrane electrode assembly required for various electrochemical energy conversion/storage devices.

■ ASSOCIATED CONTENT

Supporting Information

The Supporting Information is available free of charge at https://pubs.acs.org/doi/10.1021/acsomega.1c06128.

Linear sweep voltammograms used for ECSA calculation; EDS mapping of the Cu/PVdF-HFP; schematics of the PVdF-HFP with α-, β-, γ-phases; XRD patterns of the pre-treated PVdF-HFP support; linear sweep voltammograms for Cu/polystyrene (Cu/PS) catalysts; Nyquist plots of the Cu/PVdF-HFP and Cu/PVdF-$HFP_{stretch\text{-}anneal}$ catalysts during OER; linear sweep voltammograms and corresponding Tafel slopes for Cu/PVdF-HFP in various KOH concentrations; XPS spectra of the C 1s photoemission lines for pristine and pre-treated Cu/PVdF-HFP catalysts; XRD patterns of Cu/PVdF-HFP before and after the OER; and comparison of the OER activity before and after the cycling test (PDF)

■ AUTHOR INFORMATION

Corresponding Author

Yu Katayama − *Department of Applied Chemistry, Graduate School of Sciences and Technology for Innovation, Yamaguchi University, Ube 755-8611, Japan;* orcid.org/0000-0002-7842-2938; Phone: +81-(0)836-85-9285; Email: yuktym@yamaguchi-u.ac.jp

Authors

Shunsaku Uchiyama − *Department of Applied Chemistry, Graduate School of Sciences and Technology for Innovation, Yamaguchi University, Ube 755-8611, Japan*

Asuka Morinaga − *Department of Applied Chemistry, Graduate School of Sciences and Technology for Innovation, Yamaguchi University, Ube 755-8611, Japan*

Hiromori Tsutsumi − *Department of Applied Chemistry, Graduate School of Sciences and Technology for Innovation, Yamaguchi University, Ube 755-8611, Japan*

Complete contact information is available at: https://pubs.acs.org/10.1021/acsomega.1c06128

Author Contributions

[+]S.U. and A.M. contributed equally.

Author Contributions

The manuscript was written with contributions from all authors. All authors have approved the final version of the manuscript.

Notes

The authors declare no competing financial interest.

■ ACKNOWLEDGMENTS

This project has received funding from the Japan Society for the Promotion of Science (JSPS) KAKENHI Grant-in-Aid for Early-Career Scientists under grant number 19K15360 (Y.K.).

■ REFERENCES

(1) Sherif, S. A.; Barbir, F.; Veziroglu, T. N. Towards a Hydrogen Economy. *Electr. J.* **2005**, *18*, 62−76.

(2) Koroneos, C.; Dompros, A.; Roumbas, G.; Moussiopoulos, N. Life Cycle Assessment of Hydrogen Fuel Production Processes. *Int. J. Hydrogen Energy* **2004**, *29*, 1443−1450.

(3) Dincer, I.; Acar, C. Review and Evaluation of Hydrogen Production Methods for Better Sustainability. *Int. J. Hydrogen Energy* **2014**, *40*, 11094−11111.

(4) Wang, M.; Wang, Z.; Gong, X.; Guo, Z. The Intensification Technologies to Water Electrolysis for Hydrogen Production - A Review. *Renewable Sustainaible Energy Rev.* **2014**, *29*, 573−588.

(5) Stamenkovic, V. R.; Strmcnik, D.; Lopes, P. P.; Markovic, N. M. Energy and Fuels from Electrochemical Interfaces. *Nat. Mater.* **2016**, *16*, 57−69.

(6) Zeng, K.; Zhang, D. Recent Progress in Alkaline Water Electrolysis for Hydrogen Production and Applications. *Prog. Energy Combust. Sci.* **2010**, *36*, 307−326.

(7) Song, F.; Bai, L.; Moysiadou, A.; Lee, S.; Hu, C.; Liardet, L.; Hu, X. Transition Metal Oxides as Electrocatalysts for the Oxygen Evolution Reaction in Alkaline Solutions: An Application-Inspired Renaissance. *J. Am. Chem. Soc.* **2018**, *140*, 7748−7759.

(8) Khan, M. A.; Zhao, H.; Zou, W.; Chen, Z.; Cao, W.; Fang, J.; Xu, J.; Zhang, L.; Zhang, J. Recent Progresses in Electrocatalysts for Water Electrolysis. *Electrochem. Energy Rev.* **2018**, *1*, 483.

(9) Fabbri, E.; Habereder, A.; Waltar, K.; Kötz, R.; Schmidt, T. J. Developments and Perspectives of Oxide-Based Catalysts for the Oxygen Evolution Reaction. *Catal. Sci. Technol.* **2014**, *4*, 3800−3821.

(10) Brauns, J.; Turek, T. Alkaline Water Electrolysis Powered by Renewable Energy: A Review. *Processes* **2020**, *8*, 248.

(11) Holladay, J. D.; Hu, J.; King, D. L.; Wang, Y. An Overview of Hydrogen Production Technologies. *Catal. Today* **2009**, *139*, 244−260.

(12) Durst, J.; Siebel, A.; Simon, C.; Hasché, F.; Herranz, J.; Gasteiger, H. A. New Insights into the Electrochemical Hydrogen Oxidation and Evolution Reaction Mechanism. *Energy Environ. Sci.* **2014**, *7*, 2255−2260.

(13) Zalitis, C. M.; Sharman, J.; Wright, E.; Kucernak, A. R. Properties of the Hydrogen Oxidation Reaction on Pt/C Catalysts at Optimised High Mass Transport Conditions and Its Relevance to the Anode Reaction in PEFCs and Cathode Reactions in Electrolysers. *Electrochim. Acta* **2015**, *176*, 763−776.

(14) Hong, W. T.; Risch, M.; Stoerzinger, K. A.; Grimaud, A.; Suntivich, J.; Shao-Horn, Y. Toward the Rational Design of Non-Precious Transition Metal Oxides for Oxygen Electrocatalysis. *Energy Environ. Sci.* **2015**, *8*, 1404−1427.

(15) She, Z. W.; Kibsgaard, J.; Dickens, C. F.; Chorkendorff, I.; Nørskov, J. K.; Jaramillo, T. F. Combining Theory and Experiment in Electrocatalysis: Insights into Materials Design. *Science* **2017**, *355*, No. eaad4998.

(16) Fang, Y. H.; Liu, Z. P. Mechanism and Tafel Lines of Electro-Oxidation of Water to Oxygen on RuO2(110). *J. Am. Chem. Soc.* **2010**, *132*, 18214−18222.

(17) Stoerzinger, K. A.; Qiao, L.; Biegalski, M. D.; Shao-Horn, Y. Orientation-Dependent Oxygen Evolution Activities of Rutile IrO2 and RuO_2. *J. Phys. Chem. Lett.* **2014**, *5*, 1636−1641.
(18) Lee, Y.; Suntivich, J.; May, K. J.; Perry, E. E.; Shao-Horn, Y. Synthesis and Activities of Rutile IrO_2 and RuO_2 Nanoparticles for Oxygen Evolution in Acid and Alkaline Solutions. *J. Phys. Chem. Lett.* **2012**, *3*, 399−404.
(19) Paoli, E. A.; Masini, F.; Frydendal, R.; Deiana, D.; Schlaup, C.; Malizia, M.; Hansen, T. W.; Horch, S.; Stephens, I. E. L.; Chorkendorff, I. Oxygen Evolution on Well-Characterized Mass-Selected Ru and RuO_2 Nanoparticles. *Chem. Sci.* **2015**, *6*, 190−196.
(20) Wang, K.; Wang, X.; Li, Z.; Yang, B.; Ling, M.; Gao, X.; Lu, J.; Shi, Q.; Lei, L.; Wu, G.; et al. Designing 3d Dual Transition Metal Electrocatalysts for Oxygen Evolution Reaction in Alkaline Electrolyte: Beyond Oxides. *Nano Energy* **2020**, *77*, 105162.
(21) Jiao, Y.; Yang, C.; Wang, H.; Zhong, Y.; Hu, Y. Optimization Strategies on the Advanced Engineering of Co-Based Nanomaterials for Electrochemical Oxygen Evolution. *J. Alloys Compd.* **2022**, *890*, 161929.
(22) Du, P.; Eisenberg, R. Catalysts Made of Earth-Abundant Elements (Co, Ni, Fe) for Water Splitting: Recent Progress and Future Challenges. *Energy Environ. Sci.* **2012**, *5*, 6012−6021.
(23) Nocera, D. G. The Artificial Leaf. *Acc. Chem. Res.* **2012**, *45*, 767−776.
(24) Zhang, J.; Liu, J.; Peng, Q.; Wang, X.; Li, Y. Nearly Monodisperse Cu_2O and CuO Nanospheres: Preparation and Applications for Sensitive Gas Sensors. *Chem. Mater.* **2006**, *18*, 867−871.
(25) Gawande, M. B.; Goswami, A.; Felpin, F.-X.; Asefa, T.; Huang, X.; Silva, R.; Zou, X.; Zboril, R.; Varma, R. S. Cu and Cu-Based Nanoparticles: Synthesis and Applications in Catalysis. *Chem. Rev.* **2016**, *116*, 3722−3811.
(26) Somorjai, G. A.; Park, J. Y. Molecular Factors of Catalytic Selectivity. *Angew. Chem. Int. Ed.* **2008**, *47*, 9212−9228.
(27) Hou, C. C.; Chen, Q. Q.; Wang, C. J.; Liang, F.; Lin, Z.; Fu, W. F.; Chen, Y. Self-Supported Cedarlike Semimetallic Cu3P Nanoarrays as a 3D High-Performance Janus Electrode for Both Oxygen and Hydrogen Evolution under Basic Conditions. *ACS Appl. Mater. Interfaces* **2016**, *8*, 23037−23048.
(28) Hou, C. C.; Wang, C. J.; Chen, Q. Q.; Lv, X. J.; Fu, W. F.; Chen, Y. Rapid Synthesis of Ultralong $Fe(OH)_3$:$Cu(OH)_2$ Core-Shell Nanowires Self-Supported on Copper Foam as a Highly Efficient 3D Electrode for Water Oxidation. *Chem. Commun.* **2016**, *52*, 14470−14473.
(29) Liu, X.; Cui, S.; Qian, M.; Sun, Z.; Du, P. In Situ Generated Highly Active Copper Oxide Catalysts for the Oxygen Evolution Reaction at Low Overpotential in Alkaline Solutions. *Chem. Commun.* **2016**, *52*, 5546−5549.
(30) Liu, X.; Cui, S.; Sun, Z.; Ren, Y.; Zhang, X.; Du, P. Self-Supported Copper Oxide Electrocatalyst for Water Oxidation at Low Overpotential and Confirmation of Its Robustness by Cu K-Edge X-Ray Absorption Spectroscopy. *J. Phys. Chem. C* **2016**, *120*, 831−840.
(31) Zhou, Z.; Li, X.; Li, Q.; Zhao, Y.; Pang, H. Copper-Based Materials as Highly Active Electrocatalysts for the Oxygen Evolution Reaction. *Mater. Today Chem.* **2019**, *11*, 169−196.
(32) Zhang, H.; Jiang, H.; Xu, Q.; Hu, Y.; Li, C. Rapid Low-Temperature Synthesis of Hollow CuS0.55 Nanoparticles for Efficient Electrocatalytic Water Oxidation. *Chem. Eng. Sci.* **2019**, *195*, 665−670.
(33) Li, C.; Zhang, B.; Li, Y.; Hao, S.; Cao, X.; Yang, G.; Wu, J.; Huang, Y. Self-Assembled Cu-Ni Bimetal Oxide 3D in-Plane Epitaxial Structures for Highly Efficient Oxygen Evolution Reaction. *Appl. Catal., B* **2019**, *244*, 56−62.
(34) Ghouri, Z. K.; Badreldin, A.; Elsaid, K.; Kumar, D.; Youssef, K.; Abdel-Wahab, A. Theoretical and Experimental Investigations of Co-Cu Bimetallic Alloys-Incorporated Carbon Nanowires as an Efficient Bi-Functional Electrocatalyst for Water Splitting. *J. Ind. Eng. Chem.* **2021**, *96*, 243−253.
(35) Ashok, A.; Kumar, A.; Matin, M. A.; Tarlochan, F. Probing the Effect of Combustion Controlled Surface Alloying in Silver and Copper towards ORR and OER in Alkaline Medium. *J. Electroanal. Chem.* **June 2018**, *2019*, 66−77.
(36) Handoko, A. D.; Deng, S.; Deng, Y.; Fai Cheng, A. W.; Chan, K. W.; Tan, H. R.; Pan, Y.; Tok, E. S.; Sow, C. H.; Yeo, B. S. Enhanced Activity of H_2O_2 -Treated Copper(Ii) Oxide Nanostructures for the Electrochemical Evolution of Oxygen. *Catal. Sci. Technol.* **2016**, *6*, 269−274.
(37) Li, Y.; Zhou, X.; Qi, W.; Xie, H.; Yin, K.; Tong, Y.; He, J.; Gong, S.; Li, Z. Ultrafast Fabrication of Cu Oxide Micro/Nano-Structures via Laser Ablation to Promote Oxygen Evolution Reaction. *Chem. Eng. J.* **2020**, *383*, 123086.
(38) Wang, D.; Li, J.; Zhao, Y.; Xu, H.; Zhao, J. Bifunctional Cu_2S−$Co(OH)_2$ Nanotube Array/Cu Foam Electrocatalyst for Overall Water Splitting. *Electrochim. Acta* **2019**, *316*, 8−18.
(39) Li, M.; Xiong, Y.; Liu, X.; Bo, X.; Zhang, Y.; Han, C.; Guo, L. Facile Synthesis of Electrospun MFe2O4 (M = Co, Ni, Cu, Mn) Spinel Nanofibers with Excellent Electrocatalytic Properties for Oxygen Evolution and Hydrogen Peroxide Reduction. *Nanoscale* **2015**, *7*, 8920−8930.
(40) Wang, A. L.; Xu, H.; Feng, J. X.; Ding, L. X.; Tong, Y. X.; Li, G. R. Design of Pd/PANI/Pd Sandwich-Structured Nanotube Array Catalysts with Special Shape Effects and Synergistic Effects for Ethanol Electrooxidation. *J. Am. Chem. Soc.* **2013**, *135*, 10703−10709.
(41) Wang, Q.; Huang, X.; Zhao, Z. L.; Wang, M.; Xiang, B.; Li, J.; Feng, Z.; Xu, H.; Gu, M. Ultrahigh-Loading of Ir Single Atoms on NiO Matrix to Dramatically Enhance Oxygen Evolution Reaction. *J. Am. Chem. Soc.* **2020**, *142*, 7425−7433.
(42) Grimaud, A.; May, K. J.; Carlton, C. E.; Lee, Y. L.; Risch, M.; Hong, W. T.; Zhou, J.; Shao-Horn, Y. Double Perovskites as a Family of Highly Active Catalysts for Oxygen Evolution in Alkaline Solution. *Nat. Commun.* **2013**, *4*, 1−7.
(43) Kuznetsov, D. A.; Han, B.; Yu, Y.; Rao, R. R.; Hwang, J.; Román-Leshkov, Y.; Shao-Horn, Y. Tuning Redox Transitions via Inductive Effect in Metal Oxides and Complexes, and Implications in Oxygen Electrocatalysis. *Joule* **2018**, *2*, 225−244.
(44) Yan, L.; Xu, Z.; Hu, W.; Ning, J.; Zhong, Y.; Hu, Y. Formation of Sandwiched Leaf-like CNTs-Co/ZnCo2O4@NC-CNTs Nanohybrids for High-Power-Density Rechargeable Zn-Air Batteries. *Nano Energy* **2021**, *82*, 105710.
(45) DeRita, L.; Resasco, J.; Dai, S.; Boubnov, A.; Thang, H. V.; Hoffman, A. S.; Ro, I.; Graham, G. W.; Bare, S. R.; Pacchioni, G.; Pan, X.; Christopher, P. Structural Evolution of Atomically Dispersed Pt Catalysts Dictates Reactivity. *Nat. Mater.* **2019**, *18*, 746−751.
(46) Li, P.; Wang, M.; Duan, X.; Zheng, L.; Cheng, X.; Zhang, Y.; Kuang, Y.; Li, Y.; Ma, Q.; Feng, Z.; Liu, W.; Sun, X. Boosting Oxygen Evolution of Single-Atomic Ruthenium through Electronic Coupling with Cobalt-Iron Layered Double Hydroxides. *Nat. Commun.* **2019**, *10*, 1−11.
(47) Morinaga, A.; Tsutsumi, H.; Katayama, Y. Electrospun Cu-Deposited Flexible Fibers as an Efficient Oxygen Evolution Reaction Electrocatalyst. *ChemPhysChem* **2019**, *20*, 2973.
(48) Bai, Y.; Fang, L.; Xu, H.; Gu, X.; Zhang, H.; Wang, Y. Strengthened Synergistic Effect of Metallic M_xP_y (M = Co, Ni, and Cu) and Carbon Layer via Peapod-Like Architecture for Both Hydrogen and Oxygen Evolution Reactions. *Small* **2017**, *13*, 1−11.
(49) Noyori, M.; Neo, Y.; Mimura, H. Single-Crystalline Poly(Vinylidene Fluoride−Trifluoroethylene) Nanofiber Webs Fabricated by Electrospinning. *Jpn. J. Appl. Phys.* **2015**, *54*, No. 021601.
(50) Barique, M. A.; Ohigashi, H. Annealing Effects on the Curie Transition Temperature and Melting Temperature of Poly(Vinylidene Fluoride/Trifluoroethylene) Single Crystalline Films. *Polymer* **2001**, *42*, 4981−4987.
(51) Zhu, P.; Zhao, Y. Effects of Electrochemical Reaction and Surface Morphology on Electroactive Surface Area of Porous Copper Manufactured by Lost Carbonate Sintering. *RSC Adv.* **2017**, *7*, 26392−26400.

https://doi.org/10.1021/acsomega.1c06128
ACS Omega 2022, 7, 10077−10086

(52) Esterly, D. M.; Love, B. J. Phase Transformation to β-Poly(Vinylidene Fluoride) by Milling. *J. Polym. Sci. Part B: Polym. Phys.* **2004**, *42*, 91−97.
(53) Andrew, J. S.; Clarke, D. R. Enhanced Ferroelectric Phase Content of Polyvinylidene Difluoride Fibers with the Addition of Magnetic Nanoparticles. *Langmuir* **2008**, *24*, 8435−8438.
(54) Boccaccio, T.; Bottino, A.; Capannelli, G.; Piaggio, P. Characterization of PVDF Membranes by Vibrational Spectroscopy. *J. Membr. Sci.* **2002**, *210*, 315−329.
(55) Cai, X.; Lei, T.; Sun, D.; Lin, L. A Critical Analysis of the α, β and γ Phases in Poly(Vinylidene Fluoride) Using FTIR. *RSC Adv.* **2017**, *7*, 15382−15389.
(56) Wan, C.; Bowen, C. R. Multiscale-Structuring of Polyvinylidene Fluoride for Energy Harvesting: The Impact of Molecular-, Micro- and Macro-Structure. *J. Mater. Chem. A* **2017**, *5*, 3091−3128.
(57) Parangusan, H.; Ponnamma, D.; Al-Maadeed, M. A. A. Stretchable Electrospun PVDF-HFP/Co-ZnO Nanofibers as Piezoelectric Nanogenerators. *Sci. Rep.* **2018**, *8*, 1−11.
(58) Wang, X.; Xu, C.; Jaroniec, M.; Zheng, Y.; Qiao, S. Z. Anomalous Hydrogen Evolution Behavior in High-PH Environment Induced by Locally Generated Hydronium Ions. *Nat. Commun.* **2019**, *10*, 1−8.
(59) Sheng, W.; Gasteiger, H. A.; Shao-Horn, Y. Hydrogen Oxidation and Evolution Reaction Kinetics on Platinum: Acid vs Alkaline Electrolytes. *J. Electrochem. Soc.* **2010**, *157*, B1529.
(60) Strmcnik, D.; Lopes, P. P.; Genorio, B.; Stamenkovic, V. R.; Markovic, N. M. Design Principles for Hydrogen Evolution Reaction Catalyst Materials. *Nano Energy* **2016**, *29*, 29−36.
(61) Farinazzo Bergamo Dias Martins, P.; Papa Lopes, P.; Ticianelli, E. A.; Stamenkovic, V. R.; Markovic, N. M.; Strmcnik, D. Hydrogen Evolution Reaction on Copper: Promoting Water Dissociation by Tuning the Surface Oxophilicity. *Electrochem. Commun.* **2019**, *100*, 30−33.
(62) Mandal, D.; Kim, K. J.; Lee, J. S. Simple Synthesis of Palladium Nanoparticles, β-Phase Formation, and the Control of Chain and Dipole Orientations in Palladium-Doped Poly(Vinylidene Fluoride) Thin Films. *Langmuir* **2012**, *28*, 10310−10317.
(63) Wang, H.; Yang, Y.; Li, Q.; Lu, W.; Ning, J.; Zhong, Y.; Zhang, Z.; Hu, Y. Molecule-Assisted Modulation of the High-Valence Co3+ in 3D Honeycomb-like CoxSy Networks for High-Performance Solid-State Asymmetric Supercapacitors. *Sci. China Mater.* **2021**, *64*, 840−851.
(64) Zhang, Z.; Wang, P. Highly Stable Copper Oxide Composite as an Effective Photocathode for Water Splitting via a Facile Electrochemical Synthesis Strategy. *J. Mater. Chem.* **2012**, *22*, 2456−2464.
(65) Yin, M.; Wu, C. K.; Lou, Y.; Burda, C.; Koberstein, J. T.; Zhu, Y.; O'Brien, S. Copper Oxide Nanocrystals. *J. Am. Chem. Soc.* **2005**, *127*, 9506−9511.
(66) Wang, J.; Deng, Q.; Li, M.; Jiang, K.; Zhang, J.; Hu, Z.; Chu, J. Copper Ferrites@reduced Graphene Oxide Anode Materials for Advanced Lithium Storage Applications. *Sci. Rep.* **2017**, *7*, 1−12.
(67) Droog, J. M. M.; Schlenter, B. Oxygen Electrosorption on Copper Single Crystal Electrodes in Sodium Hydroxide Solution. *J. Electroanal. Chem.* **1980**, *112*, 387−390.
(68) Zhong, D.; Zhao, Z.; Zhao, Q.; Cheng, D.; Liu, B.; Zhang, G.; Deng, W.; Dong, H.; Zhang, L.; Li, J.; et al. Coupling of Cu(100) and (110) Facets Promotes Carbon Dioxide Conversion to Hydrocarbons and Alcohols. *Angew. Chem.* **2021**, *133*, 4929−4935.
(69) Man, I. C.; Su, H. Y.; Calle-Vallejo, F.; Hansen, H. A.; Martínez, J. I.; Inoglu, N. G.; Kitchin, J.; Jaramillo, T. F.; Nørskov, J. K.; Rossmeisl, J. Universality in Oxygen Evolution Electrocatalysis on Oxide Surfaces. *ChemCatChem* **2011**, *3*, 1159−1165.
(70) Rossmeisl, J.; Qu, Z. W.; Zhu, H.; Kroes, G. J.; Nørskov, J. K. Electrolysis of Water on Oxide Surfaces. *J. Electroanal. Chem.* **2007**, *607*, 83−89.
(71) Yeo, B. S.; Bell, A. T. Enhanced Activity of Gold-Supported Cobalt Oxide for the Electrochemical Evolution of Oxygen. *J. Am. Chem. Soc.* **2011**, *133*, 5587−5593.
(72) Bockris, J. O. M.; Reddy, A. K. N. *Modern Electrochemistry*; Springer US: New York, 1970.
(73) Wu, L.; Guo, T.; Li, T. Machine Learning-Accelerated Prediction of Overpotential of Oxygen Evolution Reaction of Single-Atom Catalysts. *iScience* **2021**, *24*, 102398.
(74) Yang, Z.; Chen, B.; Chen, W.; Qu, Y.; Zhou, F.; Zhao, C.; Xu, Q.; Zhang, Q.; Duan, X.; Wu, Y. Directly Transforming Copper (I) Oxide Bulk into Isolated Single-Atom Copper Sites Catalyst through Gas-Transport Approach. *Nat. Commun.* **2019**, *10*, 1−7.
(75) Wang, C.; Chi, M.; Li, D.; Strmcnik, D.; Van Der Vliet, D.; Wang, G.; Komanicky, V.; Chang, K. C.; Paulikas, A. P.; Tripkovic, D.; et al. Design and Synthesis of Bimetallic Electrocatalyst with Multilayered Pt-Skin Surfaces. *J. Am. Chem. Soc.* **2011**, *133*, 14396−14403.
(76) Ghosh, S.; Das, S.; Mosquera, M. E. G. Conducting Polymer-Based Nanohybrids for Fuel Cell Application. *Polymers* **2020**, *12*, 1−19.

https://doi.org/10.1021/acsomega.1c06128
ACS Omega 2022, 7, 10077−10086